# Flow dynamics in hyper-saline aquifers:

# hydro-geophysical monitoring and modelling.

Klaus Haaken[1§], Gian Piero Deidda[2], Giorgio Cassiani[3*], Rita Deiana[4], Mario Putti[5], Claudio Paniconi[6], Carlotta Scudeler[5,6], Andreas Kemna[1]

[1] Department of Geophysics, Steinmann Institute, University of Bonn, Meckenheimer Allee 176, 53115 Bonn, Germany

[2] Dipartimento di Ingegneria Civile, Ambientale e Architettura, Università di Cagliari, Via Marengo 2, 09123 Cagliari, Italy

[3] Dipartimento di Geoscienze, Università di Padova, Via Gradenigo 6, 35131 Padova, Italy

[4] Dipartimento di Beni Culturali, Università di Padova, Piazza Capitaniato 7, Palazzo Liviano, 35139 Padova, Italy

[5] Dipartimento di Matematica, Università di Padova, Via Trieste 63, 35121 Padova, Italy

[6] Institut national de la recherche scientifique, Centre Eau Terre Environnement, Université du Québec, Rue de la Couronne 490, G1K 9A9 Québec, Canada

* Corresponding author: giorgio.cassiani@unipd.it

§ currently at Björnsen Consulting Engineers, Maria Trost 3, 56070 Koblenz, Germany

20    **Abstract**

21    Saline-freshwater interaction in porous media is a phenomenon of practical interest

22    particularly for the management of water resources in arid and semi-arid environments,

23    where precious freshwater resources are threatened by seawater intrusion and where storage

24    of freshwater in saline aquifers can be a viable option. Saline-freshwater interactions are

25    controlled by physico-chemical processes that need to be accurately modelled. This in turn

26    requires monitoring of these systems, a non-trivial task for which spatially extensive, high

27    resolution non-invasive techniques can provide key information. In this paper we present the

28    field monitoring and numerical modelling components of an approach aimed at

29    understanding complex saline-freshwater systems. The approach is applied to a freshwater

30    injection experiment carried out in a hyper-saline aquifer near Cagliari (Sardinia, Italy). The

31    experiment was monitored using time-lapse cross-hole electrical resistivity tomography

32    (ERT). To investigate the flow dynamics, coupled numerical flow and transport modeling of

33    the experiment was carried out using an advanced 3D density-driven flow-transport

34    simulator. The simulation results were used to produce synthetic ERT inversion results to be

35    compared against real field ERT results. This exercise demonstrates that the evolution of the

36    freshwater bulb is strongly influencedby the system's (even mild) hydraulic heterogeneities.

37    The example also highlights how the joint use of ERT imaging and gravity dependent flow

38    and transport modelling give fundamental information for this type of studies.

39    **Keywords:** Electrical resistivity tomography; Density-driven flow; Freshwater injection;

40    Hyper-saline; Cross-hole ERT; Flow and transport modeling

## 1. INTRODUCTION

Multiphase flow in porous media has been the subject of intensive study for many decades, motivated, amongst other factors, by important economic considerations linked to the petroleum industry. Another field where interaction of pore fluids having different physical properties is particularly important is saline-freshwater systems. In this case, important density and viscosity differences between saline and fresh waters control the relative motion and mixing of the two phases. Characterizing and modelling these coupled flow and transport phenomena is a very challenging task, particularly in the presence of the hydraulic heterogeneities always present in natural porous media (e.g. Werner et al., 2013; Ketabchi et al., 2016).

The most common situation where saline-freshwater systems have practical environmental and socio-economic implications is related to seawater intrusion in coastal aquifers, often exacerbated by overexploitation of groundwater, particularly in arid and semi-arid regions such as those surrounding the Mediterranean basin (e.g. Kallioras et al., 2010; Rey et al., 2013; Dentoni et al., 2015). Another context where the study of saline-freshwater interactions is highly important is the injection and storage of freshwater in brackish or salty aquifers for later use in agriculture or for domestic purposes, also known as aquifer storage and recovery (ASR;- e.g., Pyne, 1995; Dillon, 2005).

Many studies of density-dependent flow and transport phenomena in porous media have been conducted over the past decades (e.g. Gambolati et al., 1999; Simmons et al., 2001; Diersch and Kolditz, 2002). Instabilities and fingering can take place when denser water overlies lighter water (e.g., Simmons et al., 2001). Ward et al. (2007) give an introductive literature review on density-dependent modeling, with a particular focus on ASR. The first studies on the injection of freshwater into a saline aquifer were performed by Bear and Jacobs (1965)

and Esmail and Kimbler (1967). The latter investigated the tilting of the saltwater-freshwater interface, a phenomenon known as "buoyancy stratification". More recent studies have analyzed the efficiency of ASR for both field and synthetic cases (e.g., Kumar and Kimbler, 1970; Moulder, 1970; Kimbler et al., 1975; Ward et al., 2007, 2008; Lu et al., 2011; Zuurbier et al., 2014). Ward et al. (2008) conducted a numerical study to evaluate the efficiency of ASR under density-dependent conditions with anisotropy and heterogeneity of high and low permeable layers. Van Ginkel et al. (2014) studied the possibility to extract saltwater below the freshwater injection to prevent the freshwater from floating upwards. Alaghmand et al. (2015) investigated fresh river water injection into a saline floodplain aquifer and developed a numerical model for the optimization of injection scenarios.

The behavior of saline-freshwater systems becomes increasingly complex with larger density and viscosity contrasts. To date, very little research has been done on the effects of freshwater injection in highly saline aquifers that can reach total dissolved solids (TDS) concentrations of 100 g/l. Understanding these complex systems is limited not only by the need to develop non-trivial coupled flow and transport models but also by the scarce availability of effective monitoring techniques. The latter are, under field conditions, typically limited to borehole measurements that can only provide point information in spatially heterogeneous hydraulic systems with time-changing salt concentrations.

As in many other subsurface characterization problems, a major contribution can be made by non-invasive, spatially extensive, geophysical techniques. In particular, electrical and electromagnetic methods are very suitable in the context of saline-freshwater interactions, since electrical conductivity varies over orders of magnitude depending on solute concentrations. While the use of these methods is common in seawater intrusion studies (e.g., Goldman and Kafri, 2006; Nguyen et al., 2009)., only few studies have used geophysics to monitor ASR experiments. Davis et al. (2008) used time-lapse microgravity surveys to

monitor the utilization of an abandoned coal mine as an artificial ASR site. Maliva et al. (2009) investigated the use of geophysical borehole logging tools applied to managed aquifer recharge systems, including ASR, to improve the characterization of aquifer properties. Minsley et al. (2011) developed an integrated hydrogeophysical methodology for the siting, operation, and monitoring of ASR systems using electrical resistivity, time-domain electromagnetics, and seismic methods. Parsekian et al. (2014) applied geoelectrical imaging of the subsurface below an aquifer recharge and recovery site alongside with hydrochemical measurements to identify preferential flow paths.

A major step forward in saline-freshwater systems monitoring can be made by improving the efficiency of advanced geophysical techniques, and electrical tomographic methods in particular. Electrical resistivity tomography (ERT) is widely used today in hydrogeological and environmental investigations. Often applied in  tracer studies (e.g., Kemna et al., 2002; Vanderborght et al., 2005; Cassiani et al., 2006; Doetsch et al., 2012), ERT is a natural choice for saline-freshwater interaction monitoring, given the correlation between the salinity of a pore fluid and its electrical conductivity. Time-lapse ERT, where only the changes in electrical conductivity over time are imaged (e.g., Kemna et al., 2002; Singha and Gorelick, 2005; Perri et al., 2012), can be especially effective in tracking dynamic processes. Whereas tracer studies are typically designed with injection of a saline tracer into fresh surrounding groundwater, only very few studies have dealt with the inverse case of freshwater injection into a saline formation. For instance, Müller et al. (2010) conducted tracer tests using also a less dense tracer with lower electrical conductivity than the ambient groundwater, monitored with ERT.

The goal of this study is to present a general approach for the characterization, monitoring, and modelling of complex saline-freshwater systems, based on the combination of non-invasive techniques and accurate numerical modelling. To our knowledge, no such a

116   comprehensive hydro-geophysical approach concerning freshwater injection in saline

117   aquifers has been presented so far in the scientific literature, thus we believe this case study

118   can be very useful as a starting point for other, more comprehensive methodical testing.  In

119   this study we limit ourselves to integrating field data and modelling in a loose manner, with

120   no aim at this stage to develop a full data assimilation framework, as implemented elsewhere

121   for simpler systems (e.g., Manoli et al., 2015; Rossi et al., 2015). The key message that can

122   be derived from the joint use of advanced field techniques and advanced numerical modeling

123   is nonetheless apparent in the presented case study, and more complete assimilation

124   approaches are possible provided that the advantages and limitations of the individual

125   components (data and models) are fully understood as shown in the present paper.

126   The approach is presented in the context of a case study where we injected freshwater into a

127   hyper-saline aquifer in the Molentargius Saline Regional Park in southern Sardinia, Italy. The

128   experiment was monitored using cross-hole time-lapse ERT. To investigate the mixing

129   processes, the resulting ERT images are compared with the results of a synthetic numerical

130   study of the same experiment. We consider here both homogeneous and heterogeneous

131   (layered) systems . For a quantitative comparison between the field and synthetic studies,

132   spatial moments of the freshwater bulb are calculated.

133   **2.  FIELD EXPERIMENT**

134   **2.1 Site description**

135   The Molentargius Saline Regional Nature Park is located west of Cagliari in southern

136   Sardinia, Italy (Figure 1). The park is a wetland situated very close to the coastline. The

137   exceptional nature of the site is given by the presence of both freshwater and salty water

138   basins separated by a flat area with mainly dry features (called 'Is Arenas'). The freshwater

139    areas include two ponds that originated as meteoric water retention basins. The salty water

140    areas include the stretches of water of the former system of the Cagliari salt pans.

141    The park area is characterized by an anoligo-miocenic sedimentary succession of some

142    hundreds of meters (Ulzega and Hearty, 1986) overlaid by pleistocenic deposits of marine

143    and continental origin and by alluvial and offshore bar deposits whose origin is still debated

144    (Coltorti et al., 2010; Thiel et al., 2010). This ongoing scientific debate has implications for

145    the comprehension of the phenomenon of hyper-saltiness of the park groundwater.

146    The specific site of investigation is located in the flat dry area within the park (Is Arenas,

147    Figure 1c). The water table of the unconfined aquifer is stable at 5.2 m below ground surface

148    (b.g.s.), and practically no lateral groundwater flow and also no tidal effects are evident. The

149    sediments are composed mostly of sands, with thin layers of silty sand, clayey sand, and silty

150    clay (Figure 2). The groundwater reaches salinity levels as high as three times the NaCl

151    concentration of seawater. Such high salt concentration is likely the long-term legacy of

152    infiltration of hyper-saline solutions from the salt pans dating back, in this area, to Roman

153    times. Electrical conductivity fluid logs (see Figure 3) recorded in boreholes allowed two

154    zones to be discriminated, with a transitional layer in between: (1) from the water table to a

155    depth of 6.5 m the water electrical conductivity is about 2 S/m; (2) below 12 m depth the

156    water electrical conductivity reaches 18.5 S/m. Note that Figure 3 also reports the time-lapse

157    evolution of the vertical electrical resistivity profile as a result of the freshwater injection

158    described in the following section.

159    **2.2 Freshwater injection**

160    Five boreholes for ERT measurements were drilled with 101 mm inner diameter to a depth of

161    20 m and positioned in the shape of a square with 8 m sides (4 corner boreholes) and one

162    borehole at the center (Figure 1b). All boreholes are equipped with a fully screened PVC pipe

163    (screen with 0.8 mm size).

164    In November 2011 19.4 $m^3$ of freshwater with an electrical conductivity of 0.03 S/m, stored

165    in a tank, was injected into the saline aquifer. This was done through the central borehole

166    using a double packer system with an injection segment of 1 m length. The injection chamber

167    was set between 13 m and 14 m b.g.s. The injection rate was entirely controlled by the natural

168    pressure gradient, given by the water head in the tank and the depth of injection (i.e., 13 m to

169    14 m b.g.s. plus 2 m head in the tank above the surface). The natural pressure gradient

170    provided for an initial injection rate of 0.5 l/s. However, during injection (after about 1.5 h)

171    this rate immediately rose to a rate of about 2.75 l/s. We assume that this was due to a

172    clogging of the backfill material which was "de-clogged" after 1.5 h. In total, discharging the

173    tank took about four hours.

174

175    **2.3 ERT monitoring**

176    The direct electrical conductivity measurements described in the previous subsection

177    correspond to the data that would be available as a result of a standard monitoring plan, and is

178    highly insufficient for drawing any conclusions concerning the processes that take place

179    during and after freshwater injection. The available dataset was great enriched by ERT

180    measurements, described below.

181    *Data acquisition*

182    Time-lapse ERT monitoring was applied during the injection experiment in order to image

183    the developing freshwater bulb, "visible" thanks to its lower electrical conductivity compared

184    to the surrounding saltwater. Each borehole bears externally to the casing 24 stainless steel

185  cylindrical electrodes, permanently installed from 0.6 m to 19 m depth with 0.8 m separation,

186  with the exception of the central borehole where the first electrode is placed at the surface

187  and the last at 18.4 m depth. ERT measurements were carried out in a 2D fashion, along two

188  vertical planes diagonal along the boreholes, i.e., one plane was using the borehole numbers

189  1, 5, and 3 and the second plane the borehole numbers 2, 5, and 4 (see Figure 1b), thus

190  making use of 72 electrodes per plane. This choice, in contrast to a full 3D acquisition, was

191  predicated on minimizing the acquisition time, given that the freshwater/saltwater movement

192  was expected to be relatively rapid.

193  The ERT measurements were conducted using a Syscal Pro and adopting different

194  configuration setups, consisting of in-hole dipole-dipole measurements in a skip-zero mode

195  (i.e., adjacent electrodes form a dipole) and cross-hole dipole-dipole (hereafter referred to as

196  bipole-bipole) measurements (Figure 4). Measurements were collected in normal and

197  reciprocal configurations (i.e., exchanging the current and potential dipoles) for estimation of

198  data errors. . The acquisition for one complete measurement frame (consisting of roughy

199  7,300 individual readings) required about 40 minutes.

200  ERT data were acquired in a time-lapse manner to investigate the changes over time caused

201  by the electrical conductivity changes of the developing freshwater bulb within the saline

202  aquifer. The first time step, T0, was acquired before the start of injection in order to compare

203  the following individual time steps with the background image. These were measured on the

204  day of injection, one day after injection, and five days after injection.

205  *Data processing and time-lapse ERT inversion*

206  Due to technical errors (such as bad connection of electrodes, problems with power supply)

207  and varying data quality, the ERT data were processed prior to inversion. In particular, data

208  having a misfit larger than 5% between normal and reciprocal readings were removed.

209    The temperature difference between the groundwater (21 °C) and the injected freshwater

210    (18 °C) was relatively small. Changes in electrical conductivity due to temperature effects are

211    in this case about 5% (see, e.g., Sen and Goode, 1992). Compared to the variation in

212    electrical conductivity between the two fluids, which is about three orders of magnitude, the

213    temperature effect is considered negligible.

214    The ERT field data from the freshwater injection experiment were inverted using the

215    smoothness-constraint inversion code CRTomo. A full description of the code is given by

216    Kemna (2000). In the inversion, the data errors are represented according to a linear model

217    expressed as $\varepsilon = a/R + b$, where $R$ is the measured electrical resistance. For the case at hand

218    the error parameters $a$ (absolute) and $b$ (relative) were set to 0.0001 $\Omega m$ and 10%,

219    respectively.

220    Resistivity images exhibit a variable spatial resolution (e.g., Ramirez et al., 1995; Alumbaugh

221    and Newman, 2000; Nguyen et al., 2009). A useful indicator for this variation is the

222    cumulative sensitivity $\mathbf{s}$ (e.g., Kemna et al., 2002; Nguyen et al., 2009). The sensitivity

223    indicates how a change in electrical resistivity of a certain model cell affects a transfer

224    resistance measurement. Analogously, the cumulative sensitivity quantifies the change of a

225    complete dataset to a changing model cell, and its analysis is an important step in the

226    inversion process. Note that an objective choice for a threshold, that identifies zones where

227    "reliable" vs "unreliable" ERT imaging, is not feasible. In a more qualitative manner one can

228    assume, empirically, that a cumulated sensitivity clearly below 1e-3 leads to weak

229    imaging.Figure 5 shows exemplarily the cumulative sensitivity distribution for the inversion

230    of one dataset (image plane boreholes 1-5-3 at time T0, i.e., the background image). The

231    geometry of the boreholes and the electrodes, in combination with the employed

232  measurement configurations, yields a relatively good coverage within the area of interest (i.e.,

233  mainly the area around the central borehole).

234  In a time-lapse monitoring framework, one is primarily interested in the temporal changes of

235  data and parameters. Therefore, we used the "difference inversion" approach of time-lapse

236  ERT (e.g., LaBrecque and Yang, 2000; Kemna et al., 2002), where the inversion results are

237  changes with respect to the background data at time T0. The advantage of this approach is

238  that modeling errors and data errors correlated over time are cancelled out to a significant

239  degree and associated imaging artifacts that would occur in a standard inversion are

240  suppressed.

241  *ERT imaging results*

242  The ERT dataset was collected under challenging conditions, in particular as the very large

243  salinity contrasts are manifested as extreme electrical conductivity differences over space and

244  time. Large electrical conductivity can occasionally bring DC electrical currents into a

245  nonlinear (non-Ohmic) regime, which in turn can lead to violation of the conditions for the

246  reciprocity theorem (Binley et al., 1995; Cassiani et al., 2006). This has clear implications in

247  terms of data processing, as in particular the error analysis based on reciprocal resistances

248  may not guarantee that direct and reciprocal resistances are equal to each other. Filtering the

249  data according to a reciprocity discrepancy equal to the data error level chosen for the

250  inversion (see above) meant that a fairly large percentage of the data (about 50%) were

251  rejected. Nonetheless a large volume of resistance data was still retained (nearly two

252  thousand  values per time instant).

253  The very high electrical conductivity of the system, which is characteristic of this experiment,

254  has also another consequence: separated inversion of the different electrode configurations

255  (dipole-dipole and bipole-bipole) showed that the bipole-bipole configurations provide better

256   overall results than the dipole-dipole configuration results (not shown here). This is not a

257   common situation, as observed elsewhere in situations of standard resistivity ranges (e.g.,

258   Deiana et al., 2007, 2008), where dipole-dipole data provide higher resolution images than

259   bipole-bipole data that generally only give smoother images as information is averaged over

260   large volumes. In the case shown here, for an in-hole current dipole, the current lines will not

261   penetrate far away from the borehole as they are short-circuited by the large electrical

262   conductivity of saline water surrounding at all times the external boreholes, while for the

263   cross-hole current bipole the current lines "have to" penetrate through the volume between

264   the boreholes. Thus, the sensitivity for the dipole-dipole configurations decreases very

265   strongly with increasing distance from the boreholes. However, the dipole-dipole

266   configuration still manages to provide high sensitivity in the area close to the central

267   borehole, particularly at measurement times where the freshwater bulb surrounds this

268   borehole. Hence, the data coming from both configurations were used for inversion.

269   Figure 6 shows the background image (time T0) before the start of freshwater injection. The

270   electrical resistivity of the saturated zone is very low and vertical changes due to layering of

271   lithologies are not visible. Only a gradual change to higher resistivities in the upper part just

272   below the water table can be seen. This can partly be attributed to the smoothness-constraint

273   applied in ERT inversion. However this feature is also consistent with background

274   conductivity logs (Figure 3).

275   The obtained time-lapse ERT images of the freshwater injection experiment are shown in

276   Figure 7: the distribution of the injected freshwater in the aquifer surrounding the central

277   borehole is clearly visible, in agreement with the time-lapse conductivity logs in Figure 3.

278   The very fast vertical migration of the freshwater plume is also apparent. Between 2 and 6 h

279   after the start of injection, the injection borehole (and its surroundings) is nearly totally filled

280   with freshwater, as confirmed by Figure 3 (after 5 h). However, from the ERT images the

281     freshwater also seems to move downwards below the injection chamber. A few hours after

282     injection, the freshwater plume nearly disappeared in the ERT images, and one day after

283     injection the ERT image seems to have gone back to the background situation (as also

284     confirmed by the conductivity logs in Figure 3).

285     At about 10 m to 11 m depth the difference images show a separation of the plume into two

286     parts. A layer of finer sediments (see Figure 2) is likely to cause this separation. Note that the

287     overall high electrical conductivity masks these lithological differences in the background

288     ERT images. This fine layer is a hydraulic barrier that forces freshwater to flow even more

289     through the preferential flow path provided by the borehole itself and its surrounding gravel

290     pack. Above the fine layer the plume expands again due to the larger hydraulic conductivity

291     of the coarser sediments.

292     During the experiment, the water table as well as the electrical conductivity and the

293     temperature of the borehole fluid were measured manually in all five boreholes. The water

294     table rose about 1.5 m in the injection borehole and about 0.2 m in the surrounding four

295     boreholes. The electrical conductivity log of the central borehole before, during, and after

296     injection is shown in Figure 3. It can be observed that during injection (i.e., about 1 h after

297     start of injection), the saltwater in the borehole was pushed up by freshwater. Shortly after

298     injection stopped (5 h after start of injection) the freshwater filled the entire borehole length,

299     whereas it is visible that the saltwater already entered the borehole in the bottom part (at

300     about 16 m depth) and made its way upwards. One day after the injection experiment, the

301     fluid electrical conductivities  in the central borehole were practically back to their initial

302     values, with small differences between 8 m and 14 m depth still visible. The electrical

303     conductivities of the fluid in the four corner boreholes showed only small changes that

304     nonetheless indicate that part of the freshwater bulb also reached the outer boreholes.

## 3. SYNTHETIC EXPERIMENT

In order to investigate the behavior of the injected freshwater bulb, and assess in particular the influence of the subsurface hydraulic properties on the bulb evolution, we performed a synthetic study based on the field experiment. This was undertaken using a density-dependent flow and transport simulator. Given the computational burden of the simulations, and our goal of examining in detail some of the governing parameters, we did not use a data assimilation approach at this stage, opting instead for analyses of specific scenarios. We considered four scenarios of hydraulic conductivity distribution, and compared the simulated results to each other and with the field evidence in order to gain some first insights on the dynamic response of the hyper-saline/freshwater system.

### 3.1 Flow and transport modeling

For the coupled flow and transport modelling of the freshwater injection experiment, we used a 3D density-dependent mixed finite element-finite volume simulator (Mazzia and Putti, 2005). This algorithm was shown to be very effective in the presence of advection-dominated processes or instabilities in the flow field induced by density variations (Mazzia and Putti, 2006). Here, groundwater flow is described by Darcy's law

$$\boldsymbol{v} = -K_s \boldsymbol{\nabla}(\psi + z), \tag{1}$$

where $\boldsymbol{v}$ is the Darcy flux or velocity, $K_s$ is the saturated hydraulic conductivity tensor, $\psi$ is the pressure head and $z$ the elevation head. The hydraulic conductivity is expressed in terms of the intrinsic permeability $k$ and the properties of the fluid as

$$K_s = k \frac{\rho_0 g}{\mu_0}, \tag{2}$$

324    with $\rho_0$ the density of freshwater, $g$ the gravitational acceleration and $\mu_0$ the viscosity of

325    freshwater. For density-dependent flow, the density and viscosity of the solution are strongly

326    dependent on the concentration of the solution:

$$\rho = \rho_0 e^{\epsilon c}, \tag{3.1}$$

$$\mu = \mu_0 e^{\epsilon' c}. \tag{3.2}$$

327    Here $c$ is the normalized concentration (i.e., the ratio between the concentration of the

328    solution and the maximum concentration) and $\epsilon$ and $\epsilon'$ are the density and viscosity ratios,

329    respectively, defined as

$$\epsilon = \frac{\rho_s - \rho_0}{\rho_0}, \tag{4.1}$$

$$\epsilon' = \frac{\mu_s - \mu_0}{\mu_0}, \tag{4.2}$$

330    where $\rho_s$ and $\mu_s$ are the saltwater maximum density and viscosity, respectively. In our case,

331    the density and viscosity ratios are $\epsilon = 0.084$ and $\epsilon' = 0.28$, respectively (see also Table 1).

332    For the exponential laws in Equations 3.1 and 3.2, we used a linear approximation (i.e.,

333    $\rho = \rho_0(1 + \epsilon c)$, and $\mu = \mu_0(1 + \epsilon' c)$) to reduce the computational cost while introducing

334    only a negligible inaccuracy.

335    The mass conservation equations for the coupled flow and transport model can be written as

336    (Gambolati et al., 1999):

$$S_s(1 + \epsilon c)\frac{\partial \psi}{\partial t} = \nabla \cdot \left[ K_s \frac{1 + \epsilon c}{1 + \epsilon' c}(\nabla \psi + (1 + \epsilon c)\boldsymbol{\eta_z}) \right] - \phi\epsilon\frac{\partial c}{\partial t} + \frac{\rho}{\rho_0}q^*, \tag{5}$$

$$\boldsymbol{v} = -K_s \frac{1 + \epsilon c}{1 + \epsilon' c}(\nabla \psi + (1 + \epsilon c)\boldsymbol{\eta_z}), \tag{6}$$

$$\phi\frac{\partial c}{\partial t} = \nabla \cdot (D\nabla c) - \nabla \cdot (c\boldsymbol{v}) + qc^* + f, \tag{7}$$

337  where $S_s$ is the specific storage, $t$ is time, $\boldsymbol{\eta_z}$ is the unit vector in z direction, $\phi$ the porosity,

338  $q^*$ is a source (positive)/sink (negative) term, $\boldsymbol{v}$ is the Darcy velocity, *D is hydrodynamic*

339  *dispersion,* $c^*$ is the normalized concentration of salt in the injected/extracted fluid, and $f$ is

340  the volumetric rate of injected (positive)/extracted (negative) solute that does not affect the

341  velocity field (Mazzia and Putti, 2006).

342  For the flow and transport model we used a 3D mesh (Figure 8) with about 57,000 tetrahedral

343  elements and 10,000 nodes. The size of the mesh was a good compromise between mesh

344  resolution and computational effort. The computational domain extends for 20 m in the *x* and

345  *y* directions and 15 m in *z* direction, starting at 5 m b.g.s., thus representing only the saturated

346  zone. This choice focuses our attention on the processes of interest and reduces dramatically

347  the numerical complexity of modelling coupled flow and transport processes in variably

348  saturated porous media. However, because a water table rise was observed in the boreholes

349  during the injection experiment, we needed to account for this pressure transient in the flow

350  and transport model. Thus, we simulated a comparable injection experiment using a 3D

351  variably saturated flow simulator (Paniconi and Wood, 1993). The changing pressure values

352  due to the water table rise at 5 m depth were then taken as top boundary conditions for the

353  fully saturated flow and transport model.

354  In addition to the boundary condition described above for pressure and with $c = 0$, we set

355  Dirichlet conditions also on the lateral boundaries with a hydrostatic pressure, according to

356  the concentration dependency $\psi = -(1 + \epsilon c)z$, and Neumann no-flow conditions at the

357  bottom of the mesh. The flow and transport parameter values are given in Table 1. The

358  injection borehole was modeled as a preferential flow path by giving the corresponding cells

359  a large value of hydraulic conductivity. Also the borehole backfill material was included in

360  the simulation by giving it a slightly higher hydraulic conductivity than the surrounding

361    aquifer material. The salt concentration was given as normalized concentration with a value

362    of 1.0 for the saltwater and 0.0 for the injected freshwater. The initial conditions for the

363    concentration in the aquifer were set to honor the transition zone observed in the borehole

364    fluid conductivity log (Figure 2).

365    The conditions for the injection were set by giving the cells that represent the injection

366    chamber (between 13 m and 14 m b.g.s.) a pressure head $\psi$ 2 m higher (from 15 m to 16 m).

367    To simulate the emptying of the tank, the pressure head decreases over time, calibrated after

368    the measured injection rate in the field.

369    The immediate increase of the injection rate, observed in the field experiment, was modeled

370    by a "de-clogging" effect of the material closely surrounding the injection chamber (i.e.,

371    representing the backfill material). This was done by increasing the hydraulic conductivity of

372    the corresponding cells by about one order of magnitude after a corresponding time (i.e.,

373    about 5,000 s). The simulated and true injection rates are compared in Figure 9.

374    Diffusion processes play a minor role within the time scale of the experiment since density-

375    driven flow enhances mixing processes and is therefore far greater than diffusional transport

376    (Simmons et al., 2001). Diffusion was therefore not taken into account. Different dispersivity

377    parameters were tested and compared (modeling results not shown here); their influence is

378    not significant over the short time scale considered here. Thus, only advective transport is

379    studied.

380    To investigate the influence of heterogeneous hydraulic conductivity distributions in the

381    aquifer, four different scenarios were simulated, including one homogeneous model and three

382    different layered models, with a fine (clay-silt) layer between 10.5 and 11.5 m depth(Table

383    2). The hydraulic conductivity values for the different scenarios were calibrated manually.

**3.2 Simulation of ERT monitoring**

In order to compare, at least in a semi-quantitative manner, the observed ERT inversions with the results of the synthetic study, it is necessary to convert first the simulated normalized salt concentration from the flow-transport model into bulk electrical conductivity, for example through Archie's (1942) relationship, here expressed for saturated sediments:

$$\sigma_b = \frac{\phi^m}{a}\sigma_w \,, \tag{8}$$

where $\sigma_b$ is the bulk electrical conductivity, $a$ is a tortuosity factor, $\sigma_w$ is the electrical conductivity of the fluid, and $m$ is the cementation exponent. The formation factor $F = a/\phi^m$ accounts for the pore space geometry. Due to the high salinity of the groundwater in the present case, surface conductivity is assumed to be negligible, and thus Archie's law is safely applicable. Since core data was available from one of the boreholes, it was possible to calibrate Archie's law in the laboratory with $F = 4.6$.

The next step is to simulate the field data that would be acquired given the simulated bulk electrical conductivity. For the 3D electrical forward modeling we used the same approach as Manoli et al. (2015) and Rossi et al. (2015). The electric potential field, $\Phi$, for a current injection between electrodes at $r_{S+}$ (current source) and $r_{S-}$ (current sink) is calculated by solving the Poisson equation

$$-\nabla \cdot [\sigma_b \nabla \Phi] = I[\delta(r - r_{S+}) - \delta(r - r_{S-})] \,, \tag{9}$$

together with appropriate boundary conditions, where $\sigma_b$ is the given electrical conductivity distribution, $I$ is the injected current strength, and $\delta$ is the Dirac delta function. The mesh for the geoelectrical modeling includes the unsaturated zone, and the top boundary of the mesh (at z = 0 m) was set as a Neumann no-current boundary condition. For the lateral and bottom boundaries we used Dirichlet boundary conditions. Therefore, the mesh size was expanded in

405    all directions with respect to the hydraulic mesh, so that the influence of the fixed voltage

406    boundary conditions on the current lines was negligible.

407    The final step was to process and invert the synthetic ERT data in the same way as the field

408    data.

409    **3.3 Moment analysis**

410    In order to provide a more quantitative comparison between the field and synthetic

411    experiments, we analyzed 2D moments as defined  for example by Singha and Gorelick

412    (2005):

$$M_{ij}(t) = \iint_{\Gamma} C(x,z,t)x^i z^j dx dz \tag{10}$$

413    where $M_{ij}$ is the spatial moment of order $i,j$ between 0 and 2. $x$ and $z$ are the Cartesian

414    coordinates and $dx$ and $dz$ the pixel sizes. $\Gamma$ is the integration domain of interest. The zeroth

415    moment represents the total mass in the system while the vertical first moment, normalized

416    with respect to mass, defines the center of mass in the *z*-direction. The second moments relate

417    to the spread around the center of mass.

418    **4   RESULTS AND DISCUSSION**

419    As a first step, let us consider the results of the synthetic study. Figure 10 shows the salt

420    concentration of the flow and transport simulations for scenario 4, which represents the most

421    complex parameterization of the aquifer and is assumed to be most realistic for the test site

422    (see the site stratigraphy reported in Figure 2). A general upward motion of the injected bulb

423    is visible, with the highest velocities occurring within the injection hole. After some time, the

424    freshwater starts to enter the aquifer along the entire borehole length. Although its density is

425    much less than the density of the surrounding saltwater, the freshwater also moves

426  downwards within the borehole, pushed by the pressure gradients. The 1.2 m thick fine

427  material layer also plays a clear role in the bulb dynamics. This is   expected. In

428  correspondence to this layer the flow only takes place along the borehole and the backfill

429  material. Above the fine layer the plume expands laterally into the aquifer. Also the transition

430  between the saltwater and the upper freshwater layer above 7.4 m depth moves entirely

431  upwards since the overall movement in the model domain is upwards. One can also observe

432  in the simulation results the tilting of the freshwater-saltwater interface in the lower part of

433  the borehole as well as below the groundwater level, as described by Ward et al. (2007,

434  2008). The higher the ratio of hydraulic conductivity between the two layers, the stronger is

435  the tilting, as predicted by Ward et al. (2008) (results not shown here).

436  Figure 11 shows the inverted images for four different subsurface scenarios at time 4.2 h after

437  start of injection for the flow and transport simulations and the synthetic ERT monitoring (see

438  Table 2 for definition of the scenarios). The figure clearly shows the dramatic influence of the

439  hydraulic conductivity distribution on the shape of the freshwater bulb, both in the "real"

440  images and in the corresponding inverted ERT images. Scenario 4, which includes the fine

441  layer, is closest to the field results as already discussed above. However, scenario 3, with just

442  two layers, shows a similar behavior in terms of plume development. In general, given the

443  strong influence that hydraulic conductivity has on the results, it is conceptually possible to

444  try and infer the site's hydraulic properties on the basis of the freshwater injection

445  experiment. However it is also apparent that calibrating *in detail* the true hydraulic

446  conductivity distribution in the field experiment starting from the ERT images alone may be a

447  very challenging task. In fact, while some main features are clearly identifiable, other smaller

448  details may prove difficult to capture.

449  Indeed, the governing hydraulic effect comes from the different conductivities of the upper

450  and lower parts of the aquifer (scenarios 1 + 2 vs. 3 + 4), and the fine layer does not play such

451  an important role as expected a priori. From the simulation results it is difficult to say

452  whether scenario 3 or scenario 4 is closest to reality. However, for scenarios 1 and 2 ERT

453  clearly overestimates the extent of the freshwater plume, whereas for scenarios 3 and 4 the

454  plume extension is reconstructed quite well, in particular in the deeper region (Figure 10).

455  It is instructive to examine in detail (Figure 12) the similarities and differences between the

456  ERT field data and the reconstructed ERT images from the simulation scenario that visually

457  appears better than the others (scenario 4). The simulated ERT images show the same general

458  behavior in response to the injection process and associated plume development as the ERT

459  field results. In the field ERT images the freshwater body disappears much faster. After 24 h,

460  whereas in the field ERT images the freshwater bulb is hardly visible, the simulation still

461  shows its presence. It should be noted that in the simulations the boundary condition at the

462  well is imposed as a Dirichlet (head) condition, so flux is computed depending on the applied

463  head. We applied the head as actually measured in the injection tank. Consequently, the flow

464  is never zero, not even at the end of the experiment. On the other hand, the tilting of the

465  freshwater-saltwater interface as seen in the flow and transport model results is much less

466  visible in the ERT images.

467  The imaged resistivity changes in the field experiment show less contrast than in the synthetic

468  study. The salinity difference between the freshwater and the saltwater is very large and thus

469  so is the NaCl concentration. Within this range, the electrical conductivity of the water might

470  no longer follow a linear relation with concentration (e.g., Wagner et al., 2013), while here it

471  is assumed to be linear. This can lead to a shifting in the contrast when the concentration is

472  converted into electrical conductivity.

473  Note also that the gradual change of electrical conductivity in the transition zone (i.e.,

474  between 5 m and 7.4 m depth) is not visible in the ERT images (Figure 11). In the transport

475 simulations it can be seen that this zone also moves upwards in the aquifer and becomes

476 thinner (Figure 10).

477 Another difference between the field and the synthetic ERT results is the sharpness of the

478 freshwater body: the boundaries appear smoother in the field study. Although dispersion

479 effects were not further investigated in this study, a higher value of $\alpha_L$ and $\alpha_V$ in the

480 simulations would obviously lead to a smoother gradient across the plume boundaries. On the

481 other hand, in the field results this may also be partly explained by the fact that one ERT

482 measurement frame took about 40 minutes; and since the overall plume migration was

483 relatively fast, the process is to some degree smeared in the inverted images.

484 Figure 13 shows the spatial moments ($0^{th}$ moment: total mass; $1^{st}$ moment: center of mass) of

485 the freshwater bulb for the field and synthetic ERT inversion results, as well as the "true"

486 moments from the flow and transport model (see Section 3.3). The total mass is well

487 recovered by the synthetic ERT results (using backwards the same Archie's law

488 parameterization used in the forward modelling). However, the field ERT underestimates the

489 total mass. While this is a known characteristic of moment analysis applied to ERT data for

490 tracer tests (e.g., Singha and Gorelick, 2005), in this specific case it looks likely that the

491 chosen Archie's law parameters are not fully adequate to represent the electrical

492 conductivity-salinity relationship.  Considering that even linearity of Ohm's law is

493 questionable at the high salt concentrations observed at the site, one could also question the

494 overall validity of Archie's law. Note that all other factors normally contributing to bad ERT

495 mass recovery under field conditions are the same in the synthetic and the true case, and thus

496 cannot be called into play.

497     In contrast to the total mass, the vertical center of mass is, despite some early oscillations,

498     well recovered also for the field data. This, however, is known to be a very robust indicator

499     (e.g., Binley et al., 2002; Deiana et al., 2007, 2008).

500     Overall, and in spite of the differences described above, the comparison between observed

501     and modelled ERT images is satisfactory, particularly in the face of uncertainties concerning

502     the heterogeneities of the real system that could not be investigated in extreme detail. In

503     addition, we cannot exclude the possibility that the linearity of the current flow equation may

504     be violated in such a highly conductive environment, thus leading to inconsistencies between

505     field reality and theoretical assumptions.

506     Despite the above limitations, the comparison shows that ERT imaging is a viable tool for

507     monitoring freshwater injection in a hyper-saline aquifer. This, by itself, was not an obvious

508     result. The ERT dataset was collected under extreme, challenging conditions. Even so, the

509     ERT data are of fairly good quality considering that we retained only data that passed a fairly

510     strict reciprocity check, knowing that larger reciprocity errors are likely to be related to

511     nonlinear current effects occurring in such high electrical conductivity environments. The

512     study also indicates how an accurate coupled model can mimic in an effective manner the

513     behavior of the observed freshwater bulb that was injected into the domain, and this too was

514     not self-evident.

515     **5   CONCLUSIONS**

516     In this paper we present a hydrogeophysical approach that can be used to study freshwater

517     injections in saline aquifers. In particular the approach is used to monitor and describe a

518     freshwater injection experiment conducted in a hyper-saline aquifer in the Molentargius

519     Saline Regional Park in the south of Sardinia (Italy). The experiment  was monitored using

520     time-lapse ERT in five boreholes. A numerical study of the experiment (density-dependent

521 flow and transport modeling in conjunction with ERT simulations) was carried out to

522 investigate the plume migration dynamics and the influence of different hydraulic

523 conductivity parameterizations. The numerical algorithm of the coupled flow and transport

524 model proved to be stable and accurate despite the challenging conditions.

525 The results demonstrate the feasibility and benefit of using a combination of (a) time-lapse

526 cross-borehole ERT and (b) numerical modelling of coupled flow and transport to predict the

527 same ERT results. The comparison between measured and simulated ERT images was used

528 as the key diagnostics aimed at estimating the system's governing parameters and

529 consequently describing the saltwater-freshwater dynamics. More sophisticated data

530 assimilation techniques can be used to further refine the presented approach in future work.

531 We can conclude from the present study that:

532     (a) the complex dynamics of hyper-saline/freshwater systems can be tracked using high-

533         resolution spatially extensive time-lapse non-invasive monitoring. On the contrary,

534         traditional monitoring techniques alone (e.g., conductivity logs, as in Figure 3) give

535         only a very partial image, largely inconclusive to understand the system dynamics.

536     (b) numerical modelling of these coupled systems is very challenging due to the presence

537         of strong density/viscosity contrasts and large hydraulic conductivity heterogeneities.

538         The latter in particular largely control the dynamics of the saltwater-freshwater

539         interaction. In absence of a robust numerical model it is impossible to estimate the

540         impact of hydraulic heterogeneity on this dynamics.

541     (c) a detailed comparison between field data (here, ERT time-lapse images) and modelled

542         data of the same type enables a better understanding of the behavior of a freshwater

543         bulb injected into a hyper-saline environment.

544    Our study also serves to highlight some of the weaknesses that should be addressed in future

545    work:

546    -    fine-tuning of geophysical constitutive relationships, hydraulic and transport

547         parameters, and system heterogeneities needs to be improved. We managed to bring

548         the match between field and synthetic data to an acceptable level with relatively small

549         effort, but it is very difficult to improve the match further. For instance, in the case

550         presented here the injected freshwater bulb "disappears" from the real ERT images

551         faster than in the simulation results. Also, the mass balance is honored easily in the

552         simulations while in the real data lack of mass is apparent. All of this points towards a

553         number of aspects that could be improved in the data matching. However, the target

554         parameters to be modified for this improvement are not easy to identify, given their

555         very high number and complex nature. Among these, there are hydraulic parameters

556         and dispersivities, and their spatial heterogeneities, and also Archie's law parameters.

557         This task is likely to be challenging even in a rigorous data assimilation framework,

558         and equifinality of model parameterizations is likely.

559    -    the extreme hyper-saline system considered here is likely to exceed the limits of linear

560         relationships between current and voltage (Ohm's law) as well as between electrical

561         conductivity and salinity. Therefore a full nonlinear analysis should be conducted,

562         particularly concerning the electrical behavior of the system. In absence of this, we

563         have to limit ourselves to a semi-quantitative interpretation, as shown here.

564    Finally, with regards to practical aspects of freshwater injection and monitoring in saline

565    aquifers, we can draw the following conclusions:

566    -    although in typical ASR applications the contrasts of density and salinity are usually

567         smaller, this study shows that time-lapse ERT is a powerful monitoring tool for this

568       (and also other) types of hyper-saline applications. ERT can provide spatial

569       information that is unattainable using traditional monitoring techniques (e.g., in

570       boreholes).

571    -  the movement and mixing of the freshwater plume can be very fast, thus any ERT

572       monitoring must adopt configurations for quick measurements (e.g., in the conditions

573       represented in this study an acquisition time of less than 30 minutes is recommended).

574    -  in hyper-saline systems, measuring reciprocity may not be the ideal error indicator

575       since nonlinear phenomena may be triggered, or, during the time between the normal

576       and reciprocal measurement the system may have already changed, thus invalidating

577       the reciprocity check.

578    The example shown in this paper shows how the joint use of ERT imaging and gravity

579    dependent flow and transport modelling give fundamental information for this type of

580    studies.

581 **Acknowledgements**

582 This research was supported by the Basic Research Project L.R. 7/2007 (CRP2_686, Gian

583 Piero Deidda) funded by the Regione Autonoma della Sardegna (Italy). We thank the Parco

584 Naturale Molentargius-Saline for allowing us to set up a test site in the park. We also thank

585 the field crew from the University of Cagliari (namely Luigi Noli and Mario Sitzia) as well as

586 Marco Mura, Enzo Battaglia, and Francesco Schirru for their work in the field. Special thanks

587 go to Damiano Pasetto and Gabriele Manoli for their support regarding the 3D ERT forward

588 modeling code and Annamaria Mazzia for assistance concerning the numerical experiments.

589 The data can be obtained from the authors upon request.

590

**References**

591 Alaghmand, S., Beecham, S., Woods, J. A., Holland, K. L., Jolly, I. D., Hassanli, A., Nouri,

593     H., 2015. Injection of fresh river water into a saline floodplain aquifer as a salt

594     interception measure in a semi-arid environment. Ecol. Eng. 75, 308-322,

595     doi:10.1016/j.ecoleng.2014.11.014.

596 Alumbaugh, D. L., Newman, G. A., 2000. Image appraisal for 2-D and 3-D electromagnetic

597     inversion. Geophys. 65, 1455-1467.

598 Archie, G. E., 1942. The electrical resistivity log as an aid in determining some reservoir

599     characteristics. Trans. of the Am. Inst. of Min., Metall. and Pet. Eng. 146, 54-62.

600 Bear, J., Jacobs, M., 1965. On the movement of water bodies injected into aquifers. J.Hydrol.

601     3, 37-57.

602 Binley, A., Ramirez, A., Daily, W., 1995. Regularised image reconstruction of noisy

603     electrical resistance tomography data. In: Beck, M.S., Hoyle, B.S., Morris, M.A.,

604     Waterfall, R.C., Williams, R.A. (Eds.), Process Tomography — 1995, Proceedings of

605     the 4th Workshop of the European Concerted Action on Process Tomography, Bergen,

606     6–8 April 1995, pp. 401– 410.

607 Binley A.M., G. Cassiani, R. Middleton, and P., Winship, 2002. Vadose zone flow model

608     parameterisation using cross-borehole radar and resistivity imaging, *J. Hydrol.*, 267,

609     147-159.

610 Camporese, M., Cassiani, G., Deiana, R., Salandin, P., 2011. Assessment of local hydraulic

611     properties from electrical resistivity tomography monitoring of a three-dimensional

612     synthetic tracer test experiment. Water Resour. Res. 47, W12508,

613     doi:10.1029/2011WR010528.

614    Camporese, M., Cassiani, G., Deiana, R., Salandin, P., Binley, A., 2015. Coupled and

615        uncoupled hydrogeophysical inversions using ensemble Kalman filter assimilation of

616        ERT-monitored tracer test data. Water Resour. Res. 51(5), 3277-3291,

617        doi:10.1002/2014WR016017.

618    Cassiani, G., Bruno, V., Villa, A., Fusi, N., Binley, A., 2006. A saline tracer test monitored

619        via time-lapse surface electrical resistivity tomography. J. Appl. Geophys. 59, 244-

620        259, doi:10.1016/j.jappgeo.2005.10.007.

621    Coltorti, M., Melis, E., Patta, D., 2010. Geomorphology, stratigraphy and facies analysis of

622        some Late Pleistocene and Holocene key deposits along the coast of Sardinia (Italy).

623        Quat. Int. 222, 19-35, doi:10.1016/j.quaint.2009.10.006.

624    Davis, K., Li, Y., Batzle, M., 2008. Time-lapse gravity monitoring: A systematic 4D

625        approach with application to aquifer storage and recovery. Geophys. 73(6), WA61-

626        WA69, doi:10.1190/1.2987376.

627    Deiana R., G. Cassiani, A. Kemna, A. Villa, V. Bruno and A. Bagliani, 2007. An experiment

628        of non invasive characterization of the vadose zone via water injection and cross-hole

629        time-lapse geophysical monitoring, *Near Surface Geophysics*, 5, 183-194,

630        doi:10.3997/1873-0604.2006030.

631    Deiana R., G. Cassiani, A. Villa, A. Bagliani and V. Bruno, 2008. Model calibration of a

632        water injection test in the vadose zone of the Po River plain using GPR cross-hole

633        data, doi:10.2136/vzj2006.0137 *Vadose Zone J.*, 215-226.

634    Dentoni M., R. Deidda, C. Paniconi, K. Qahman, G. Lecca, 2015, A simulation/optimization

635        study to assess seawater intrusion management strategies for the Gaza Strip coastal

636    aquifer (Palestine), *Hydrogeology Journal*, 23, 249-264; doi: 10.1007/s10040-014-

637    1214-1,

638    Diersch, H.-J. G., Kolditz, O., 2002. Variable-density flow and transport in porous media:

639    approaches and challenges. Adv. Water Resour. 25, 899-944.

640    Dillon, P., 2005. Future management of aquifer recharge. Hydrogeol. J. 13, 313-316,

641    doi:10.1007/s10040-004-0413-6.

642    Doetsch, J., Linde, N., Vogt, T., Binley, A., Green, A. G., 2012. Imaging and quantifying

643    salt-tracer transport in a riparian groundwater system by means of 3D ERT

644    monitoring. Geophys. 77(5), 207-218, doi:10.1190/GEO2012-0046.1.

645    Esmail, O. J., Kimbler, O. K., 1967. Investigation of the technical feasibility of storing fresh

646    water in saline aquifers. Water Resour. Res. 3(3), 683-695.

647    Gambolati, G., Putti, M., Paniconi, C., 1999. Three-dimensional model of coupled density

648    dependent flow and miscible salt transport, in Seawater Intrusion in Coastal Aquifers

649    – Concepts, Methods and Practices, edited by J. Bear, A. H.-D. Cheng, S. Sorek, D.

650    Ouazar, and I. Herrera, pp. 315-362, Kluwer Academic Publishers, Dordrecht, The

651    Netherlands.

652    Goldman, M., Kafri, U., 2006. Hydrogeophysical applications in coastal aquifers, in Applied

653    Hydrogeophysics, edited by H. Vereecken, A. Binley, G. Cassiani, A. Revil and K.

654    Titov, pp.233-254, Springer.

655    Kallioras A., F. Pliakas, I. Diamantis, 2010, Simulation of groundwater flow in a sedimentary

656    aquifer system subjected to overexploitation, *Water Air Soil Pollution*, 211, 177-201,

657    doi: 10.1007/s11270-009-0291-6.

658      Kemna, A., 2000. Tomographic inversion of complex resistivity - Theory and application.

659          Ph.D. thesis, Bochum Ruhr-University, Bochum, Germany.

660      Kemna, A., Vanderborght, J., Kulessa, B., Vereecken, H., 2002. Imaging and characterisation

661          of subsurface solute transport using electrical resistivity tomography (ERT) and

662          equivalent transport models. J. Hydrol. 267, 125-146, doi:10.1016/S0022-

663          1694(02)00145-2.

664      Ketabchi H., D. Mahmoodzadeh, B. Ataie-Ashtiani, C.T. Simmons, 2016, Sea-level rise

665          impacts on seawater intrusion in coastal aquifers: review and integration, *Journal of*

666          *Hydrology*, 535, 235-255, doi: 10.1016/j.jhydrol.2016.01.083.

667      Kimbler, O. K., Kazmann, R. G., Whitehead, W. R., 1975. Cyclic storage of fresh water in

668          saline aquifers. 78pp., Louisiana Water Resour. Res. Inst. Bulletin 10, Baton Rouge,

669          L.A.

670      Kumar, A., Kimbler, O. K., 1970. Effect of dispersion, gravitational segregation, and

671          formation stratification on the recovery of freshwater stored in saline aquifers. Water

672          Resour. Res. 6, 1689-1700, doi:10.1029/WR006i006p01689.

673      LaBrecque, D. J., Yang, X., 2000. Difference inversion of ERT data: a fast inversion method

674          for 3-D in-situ monitoring. Proc. Symp. Appl. Geophys. Eng. Environ. Probl.,

675          Environ. Eng. Geophys. Soc., 723-732.

676      Lu, C., Du, P., Chen, Y., Luo, J., 2011. Recovery efficiency of aquifer storage and recovery

677          (ASR) with mass transfer limitation. Water Resour. Res. 47, W08529,

678          doi:10.1029/2011WR010605.

679    Maliva, R. G., Clayton, E. A., Missimer, T. M., 2009. Application of advanced borehole geophysical logging to managed aquifer recharge investigations. Hydrogeol. J. 17(6), 1547-1556, doi:10.1007/s10040-009-0437-z.

682    Manoli, G., Rossi, M., Pasetto, D., Deiana, R., Ferraris, S., Cassiani, G., Putti, M., 2015. An iterative particle filter approach for coupled hydro-geophysical inversion of a controlled infiltration experiment. J. Comput. Phys. 283, 37-51, doi:10.1016/j.jcp.2014.11.035.

686    Mazzia, A., Putti, M., 2005. High order Godunov mixed methods on tetrahedral meshes for density driven flow simulations in porous media. J. Comput. Phys. 208, 154-174, doi:10.1016/j,jcp.2005.01.029.

689    Mazzia, A., Putti, M., 2006. Three-dimensional mixed finite element-finite volume approach for the solution of density-dependent flow in porous media. J. Comput. Appl. Math. 185(2), 347-359, doi:10.1016/j.cam.2005.03.015.

692    Minsley, B. J., Ajo-Franklin, J., Mukhopadhyay, A., Morgan, F. D., 2011. Hydrogeophysical methods for analyzing aquifer storage and recovery systems. Ground Water 49(2), 250-269, doi:10.1111/j.1745-6584.2010.00676.x.

695    Moulder, E. A., 1970. Freshwater bubbles: A possibility for using saline aquifers to store water. Water Resour. Res. 6, 1528-1531, doi:10.1029/WR006i005p01528.

697    Müller, K., Vanderborght, J., Englert, A., Kemna, A., Huisman, J. A., Rings, J., Vereecken, H., 2010. Imaging and characterization of solute transport during two tracer tests in a shallow aquifer using electrical resistivity tomography and multilevel groundwater samplers. Water Resour. Res. 46, W03502, doi:10.1029/2008WR007595.

701 Nguyen, F., Kemna, A., Antonsson, A., Engesgaard, P., Kuras, O., Ogilvy, R., Gisbert, J.,
702     Jorreto, S., Pulido-Bosch, A., 2009. Characterization of seawater intrusion using 2D
703     electrical imaging. Near Surf. Geophys. 7(5-6), 377-390, doi:10.3997/1873-
704     0604.2009025.

705 Paniconi, C., Wood, E. F., 1993. A detailed model for simulation of catchment scale
706     subsurface hydrologic processes. Water Resour. Res. 29(6), 1601-1620.

707 Parsekian, A. D., Regnery, J., Wing, A. D., Knight, R., Drewes, J. E., 2014. Geophysical and
708     hydrochemical identification of flow paths with implications for water quality at an
709     ARR site. Groundw. Monit. Remediat. 34(3), 105-116, doi:10.1111/gwmr.12071.

710 Perri, M. T., Cassiani, G., Gervasio, I., Deiana, R., Binley, A., 2012. A saline tracer test
711     monitored via both surface and cross-borehole electrical resistivity tomography:
712     Comparison of time-lapse results. J. Appl. Geophys. 79, 6-16,
713     doi:10.1016/j.jappgeo.2011.12.011.

714 Pyne, R. D. G., 1995. Groundwater recharge and wells: A guide to aquifer storage recovery.
715     CRC Press LLC, Boca Raton, Florida.

716 Ramirez, A. L., Daily, W. D., Newmark, R. L., 1995. Electrical resistance tomography for
717     steam injection monitoring and process control. JEEG 1, 39-51.

718 Rey J., J. Martínez, G.G. Barberá, J.L. García-Aróstegui, J. García-Pintado, D. Martínez-
719     Vicente, 2013, Geophysical characterization of the complex dynamics of groundwater
720     and seawater exchange in a highly stressed aquifer system linked to a coastal lagoon
721     (SE Spain), *Environ. Earth Sci.*, 70, 2271-2282, doi: 10.1007/s12665-013-2472-2.

722 Rossi, M., Manoli, G., Pasetto, D., Deiana, R., Ferraris, S., Strobbia, C., Putti, M., Cassiani,
723     G., 2015. Coupled inverse modeling of a controlled irrigation experiment using

724       multiple hydro-geophysical data. Adv. Water Resour. 82, 150-165,

725       doi:10.1016/j.advwatres.2015.03.008.

726  Sen, P. N., Goode, P. A., 1992. Influence of temperature on electrical conductivity on shaly

727       sands. Geophys. 57, 89-96.

728  Simmons, C. T., Fenstemaker, T. R., Sharp Jr., J. M., 2001. Variable-density groundwater

729       flow and solute transport in heterogeneous porous media: approaches, resolutions and

730       future challenges. J. Contam. Hydrol. 52, 245-275.

731  Singha, K., Gorelick, S. M., 2005. Saline tracer visualized with three-dimensional electrical

732       resistivity tomography: Field-scale spatial moment analysis. Water Resour. Res. 41,

733       W05023, doi:10.1029/2004WR003460.

734  Thiel, C., Coltorti, M., Tsukamoto, S., Frechen, M., 2010. Geochronology for some key sites

735       along the coast of Sardinia (Italy). Quat. Int. 222, 36-47,

736       doi:10.1016/j.quaint.2009.12.020.

737  Ulzega, A., Hearty, P. J., 1986. Geomorphology, stratigraphy and geochronology of Late

738       Quaternary marine deposits in Sardinia. Z. Geomorph. N. F. 62, 119-129.

739  Vanderborght, J., Kemna, A., Hardelauf, H., Vereecken, H., 2005. Potential of electrical

740       resistivity tomography to infer aquifer characteristics from tracer studies: A synthetic

741       case study. Water Resour. Res. 41, W06013, doi:10.1029/2004WR003774.

742  Van Ginkel, M., Olsthoorn, T. N., Bakker, M., 2014. A new operational paradigm for small-

743       scale ASR in saline aquifers. Ground Water 52(5), 685-693, doi:10.1111/gwat.12113.

744  Wagner, F. M., Möller, M., Schmidt-Hattenberger, C., Kempka, T., Maurer, H., 2013.

745       Monitoring freshwater salinization in analog transport models by time-lapse electrical

746    resistivity    tomography.    J.    Appl.    Geophys.    89,    84-95,

747        doi:10.1016/j.jappgeo.2012.11.013.

748  Ward, J. D., Simmons, C. T., Dillon, P. J., 2007. A theoretical analysis of mixed convection

749        in aquifer storage and recovery: How important are density effects?. J. Hydrol. 343,

750        169-186.

751  Ward, J. D., Simmons, C. T., Dillon, P. J., 2008. Variable-density modelling of multiple-

752        cycle aquifer storage and recovery (ASR): Importance of anisotropy and layered

753        heterogeneity    in    brackish    aquifers.    J.    Hydrol.    356,    93-105,

754        doi:10.1016/j.jhydrol.2008.04.012.

755  Werner A.D., M. Bakker, V.E.A. Post, A. Vandenbohede, C. Lu, B. Ataie-Ashtiani, C.T.

756        Simmons, D.A. Barry, 2013, Seawater intrusion processes, investigation and

757        management: recent advances and future challenges, *Adv. Water Resources*, 51, 3-26,

758        doi: 10.1016/j.advwatres.2012.03.004.

759  Zuurbier, K. G., Zaadnoordijk, W. J., Stuyfzand, P. J., 2014. How multiple partially

760        penetrating wells improve the freshwater recovery of coastal aquifer storage and

761        recovery (ASR) systems: A field and modeling study. J. Hydrol. 509, 430-441,

762        doi:10.1016/j.jhydrol.2013.11.057.

763

764 **Figures**
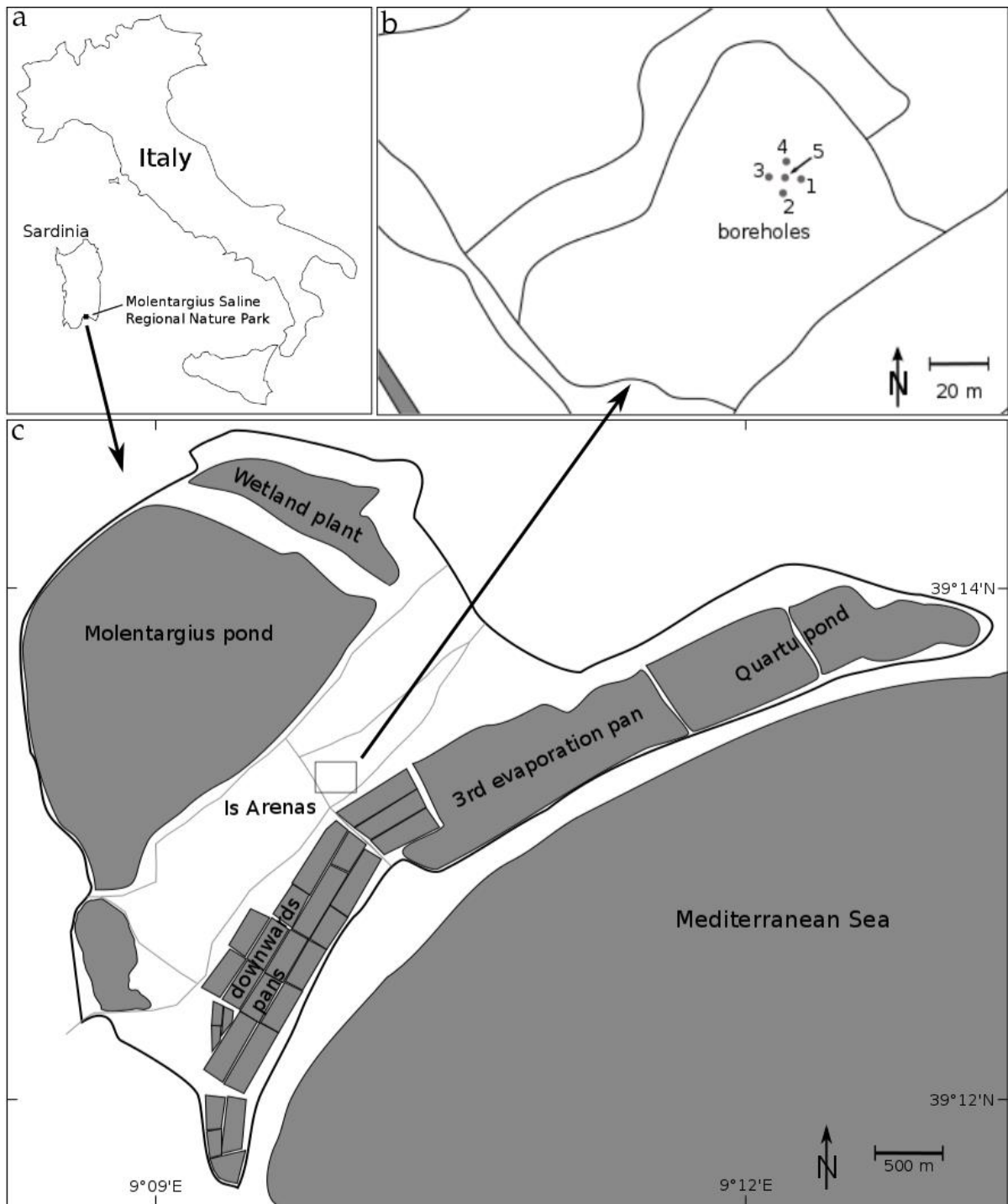
766 **Figure 1.** Geographical location of the test site: (a) Molentargius Saline Regional Nature

767 Park located East of Cagliari in southern Sardinia, Italy, (b) Detailed sketch map of location

768 and arrangement of the boreholes, (c) Sketch map of the Molentargius Park (modified after

769 google.earth).

770
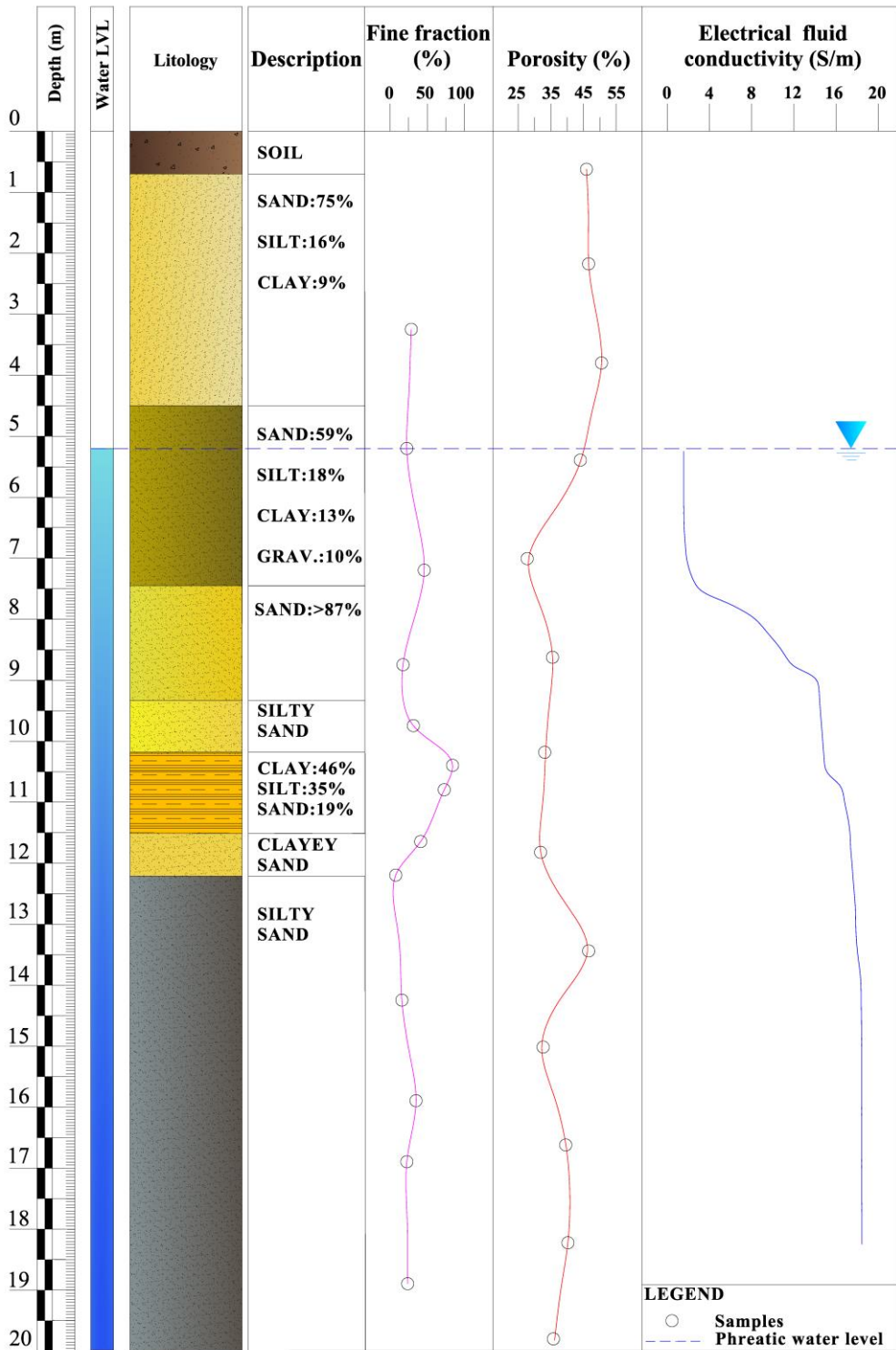
**Figure 2.** Generalized stratigraphy log from the five drilled boreholes including lithology, percentage of fine fraction, and porosity from samples as well as electrical conductivity of borehole fluid. The water table lies at 5.2 m b.g.s..

774
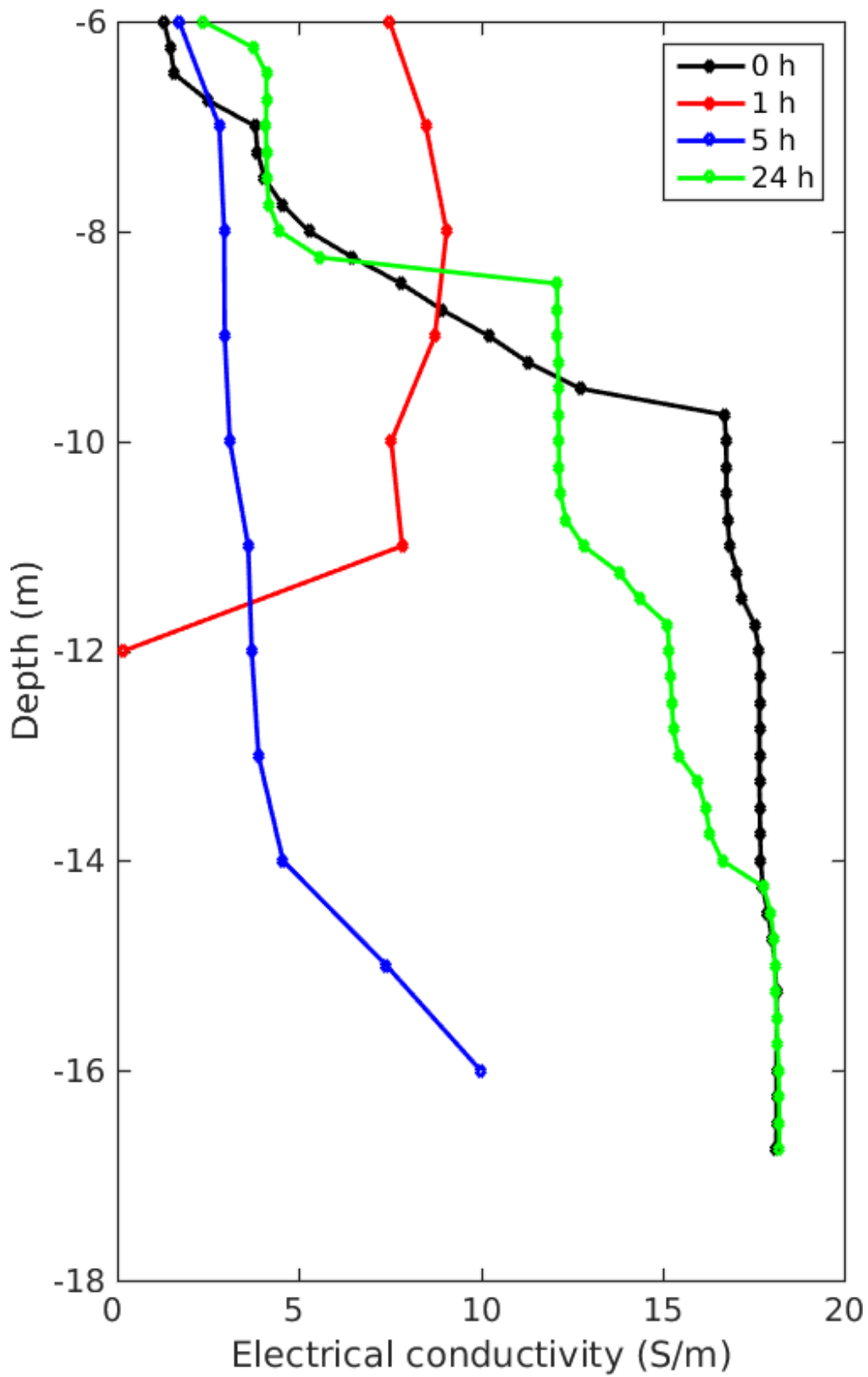
**Figure 3.** Electrical conductivity log of the fluid in borehole 5 at different times after start of

freshwater injection (section 2.2). 0 h denotes the background measurement before injection.

At 1 h there are no measurements below 12 m b.g.s. because the packer system occupied the

borehole.

779
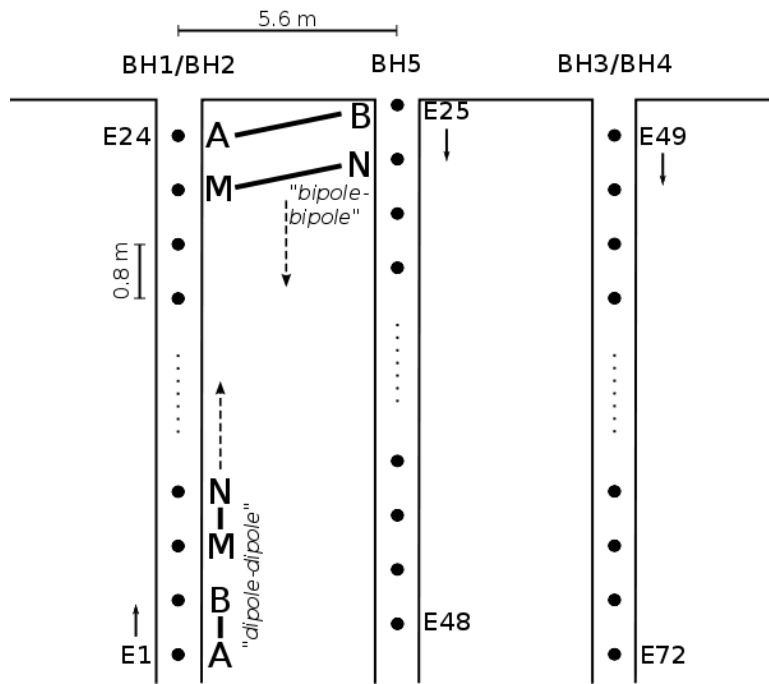
**Figure 4.** Schematic description of the ERT measurement configurations used. For dipole-dipole measurements, one dipole is always within one borehole, the other dipole also moves into the adjacent borehole. Bipole-bipole measurements are done as cross-hole measurements and are also changing as diagonals (i.e., A stays while B moves downwards for up to five electrode positions before A is also moved; similarly for M and N).

785
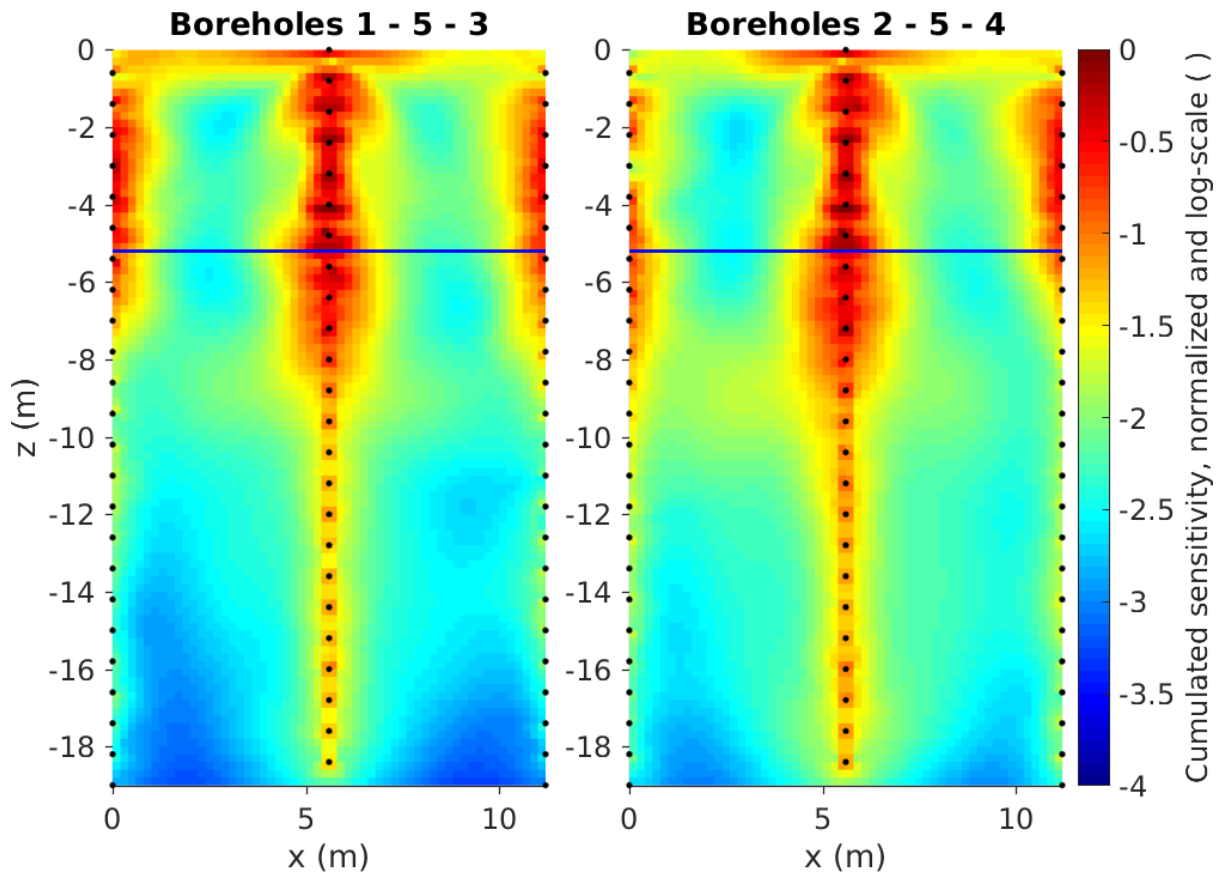
**Figure 5.** Cumulated sensitivity distribution for the inverted background (T0) dataset along plane 1 – 5 – 3.
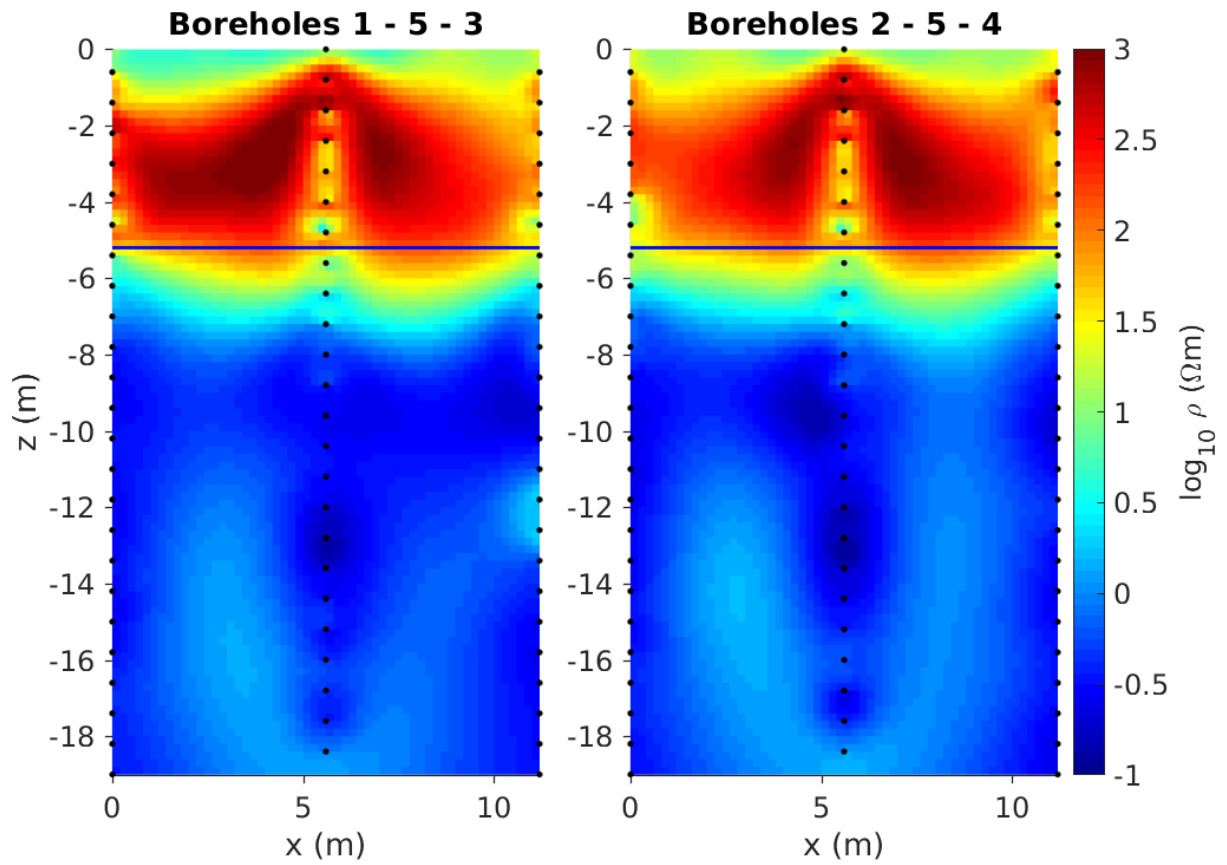
791 **Figure 6**: Inverted background (T0) image of plane $2 - 5 - 4$ including the unsaturated zone.

792 Black diamonds denote the position of the electrodes and the blue line shows the groundwater

793 table at 5.2 m b.g.s.

790

794
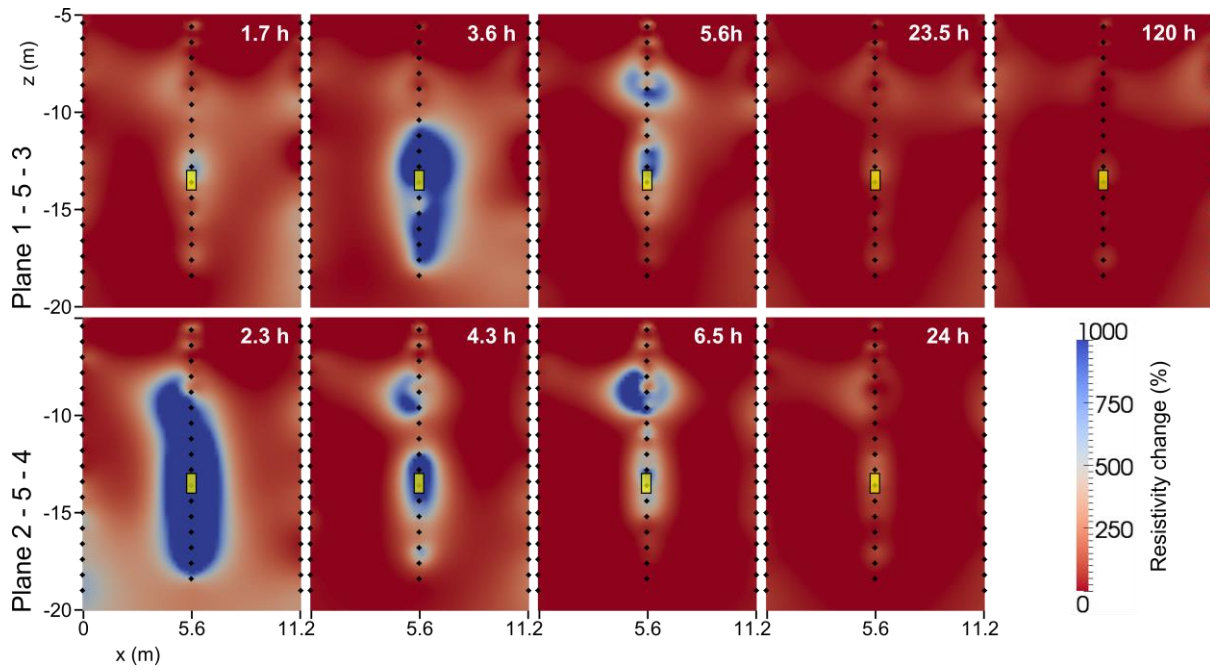
795

796

797 **Figure 7.** Electrical imaging (difference inversion) results for the field experiment at

798 different times (in h after start of injection). The top panel shows the results from borehole

799 plane 1 – 5 – 3 and the bottom panel from plane 2 – 5 – 4. Black diamonds denote the

800 position of electrodes.

801

802
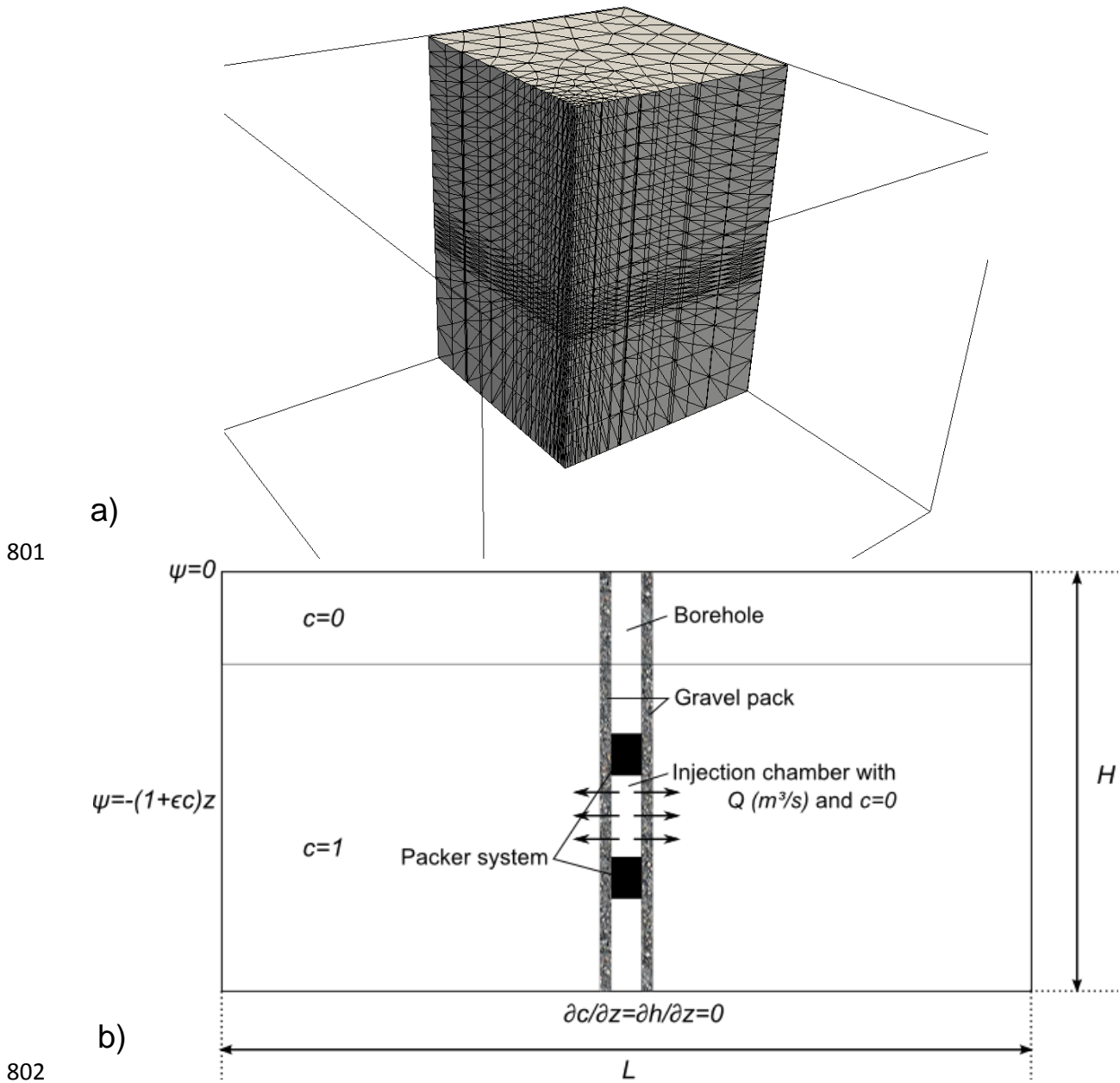
803 **Figure 8.** (a) 3D mesh with refinement in the central part and around injection layers and (b)

804 conceptual model for the synthetic injection experiment.
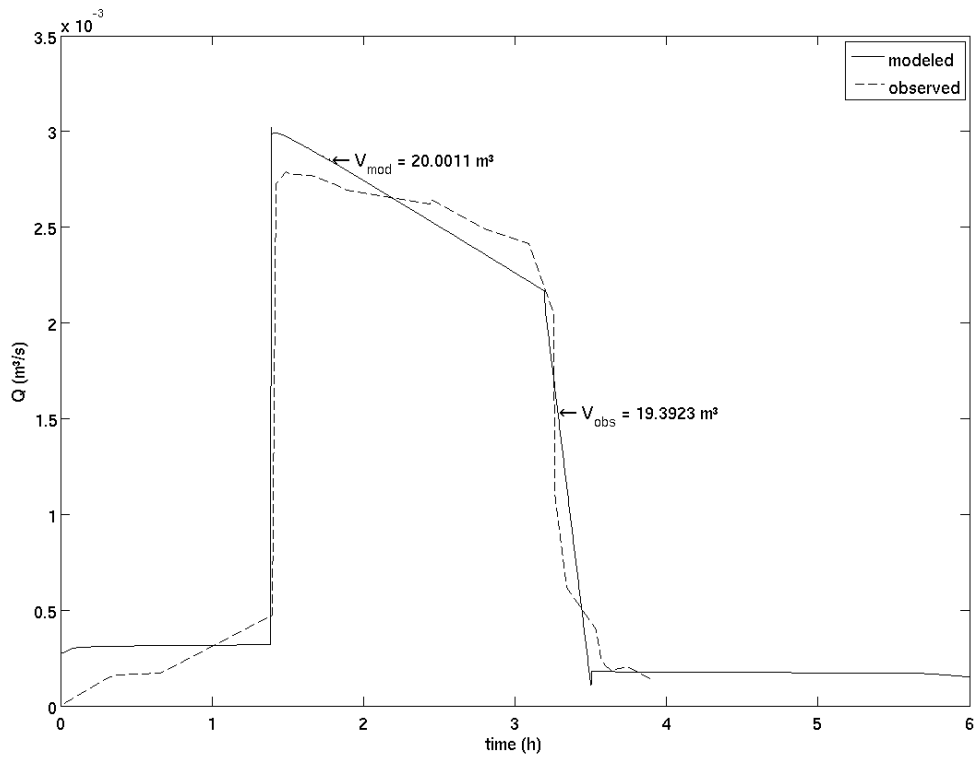
805

806 **Figure 9.** Injection rate of the experiment. The dashed line shows the observed injection in

807 the field experiment (total volume of injected water 19.4 m³) and the solid line shows the

808 calibrated injection rate of the flow and transport model.

809
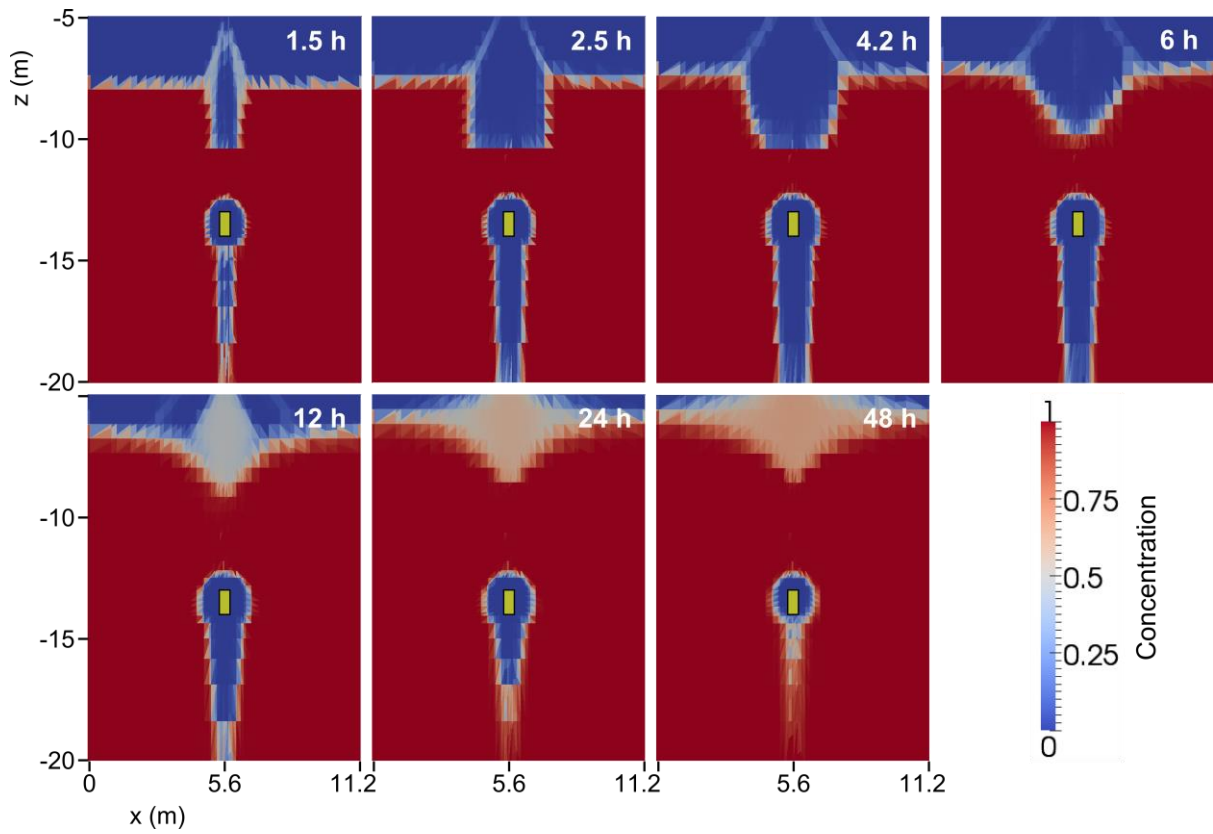
**Figure 10.** Flow and transport modeling results at different times (in h after start of injection) for scenario 4 (see Table 2).

810

811

812

813
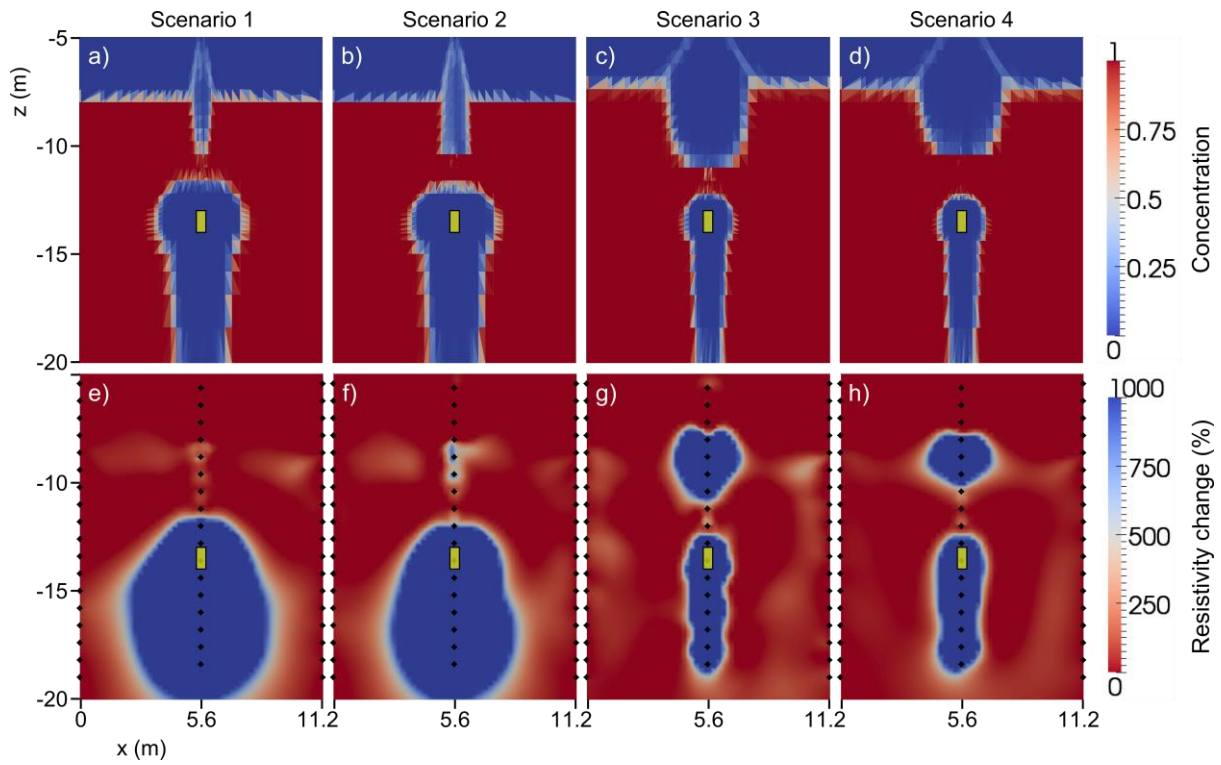
Figure 11: Comparison of simulation results for different hydraulic conductivity parameterizations at time 4.2 h after start of injection. The top panel shows the flow and transport modeling results, the bottom panel the corresponding simulated ERT results. (a) and (e) homogeneous model, (b) and (f) fine layer within homogeneous model, (c) and (g) two-layered system, and (d) and (h) two-layered system including fine layer at interface.

819
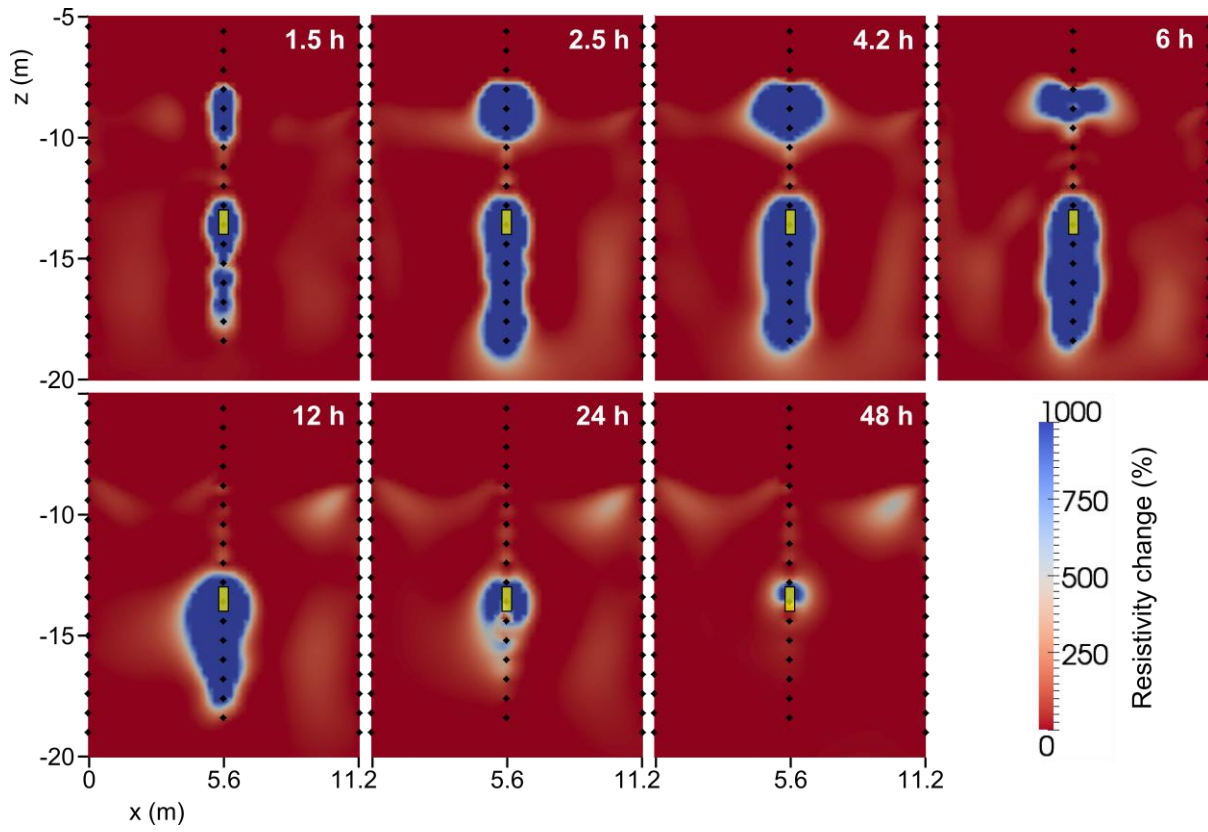
820

821 **Figure** 12: Results of synthetic ERT experiment for selected times (in h after start of

822 injection) for scenario 4 (see Table 2). Black diamonds denote the position of electrodes.
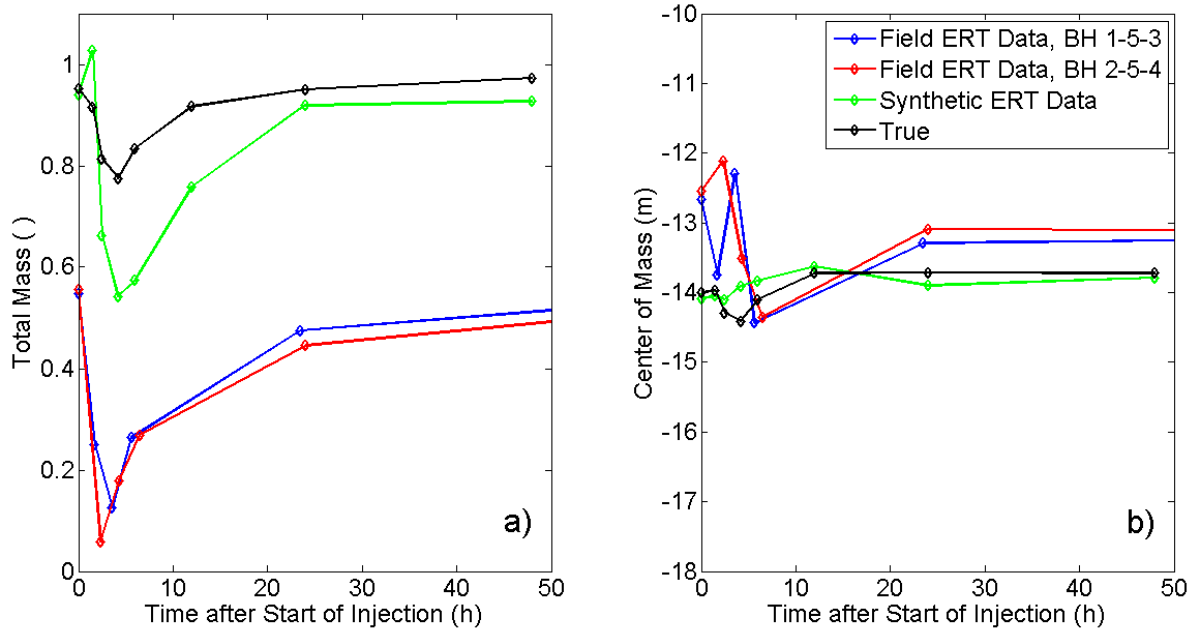
823

824    **Figure 13.** Spatial moments for the field ERT data, synthetic ERT data, and the true data

825    from the flow and transport model. The moments for the true field were calculated in 3D

826    while those for the ERT tomograms were calculated in 2D. The field ERT data are separated

827    into the two borehole planes. (a) shows the total mass in the system, normalized, and (b) is

828    the center of mass in the vertical direction.

   **Tables**

830   **Table 1.** Flow and transport input parameters for the different zones in the model.

| Parameter | Symbol | Value | Unit |
|---|---|---|---|
| **Model** | | | |
| Aquifer thickness (z direction) | H | 15 | m |
| Horizontal extent (x and y direction) | L | 20 | m |
| | | | |
| **Thickness of aquifer layers** | | | |
| Upper layer | | 5.4 | m |
| Middle layer | | 1.2 | m |
| Bottom layer | | 8.4 | m |
| | | | |
| **Hydraulic conductivities** | | | |
| *Aquifer* | | | |
| Upper layer | | $10^{-5}$-$10^{-3}$ | m s$^{-1}$ |
| Middle layer | | $10^{-6}$-$10^{-5}$ | m s$^{-1}$ |
| Bottom layer | | $10^{-5}$ | m s$^{-1}$ |
| *Well* | | | |
| Injection chamber | | $10^{-3}$ | m s$^{-1}$ |
| Packer system | | $10^{-12}$ | m s$^{-1}$ |
| Remaining well | | 1 | m s$^{-1}$ |
| *Gravel pack* | | | |
| Clogging effect | | $10^{-4}$-$10^{-3}$ | m s$^{-1}$ |
| Remaining gravel | | $10^{-2}$ | m s$^{-1}$ |
| | | | |
| **Solid and fluid properties** | | | |
| Porosity | $\phi$ | 0.35 | - |
| Longitudinal dispersivity | $\alpha_L$ | $10^{-5}$ | m |
| Transverse dispersivity | $\alpha_T$ | $10^{-5}$ | m |
| Diffusion coefficient | $D^*$ | 0 | |
| Density difference ratio | $\epsilon$ | 0.084 | - |
| Viscosity difference ratio | $\epsilon'$ | 0.28 | - |
| | | | |
| **Injection parameters** | | | |
| Injected volume | $V_{mod}$ | 20 | m³ |
| Injection duration | | 3.5 | h |

832    **Table 2.** Hydraulic conductivities of each layer for the four different scenarios.

|              | Scenario 1 | Scenario 2 | Scenario 3 | Scenario 4 |
|--------------|------------|------------|------------|------------|
| Upper layer  | $5\cdot10^{-5}$ m s$^{-1}$ | $5\cdot10^{-5}$ m s$^{-1}$ | $1\cdot10^{-3}$ m s$^{-1}$ | $1\cdot10^{-3}$ m s$^{-1}$ |
| Middle layer | $5\cdot10^{-5}$ m s$^{-1}$ | $1\cdot10^{-6}$ m s$^{-1}$ |            | $1\cdot10^{-6}$ m s$^{-1}$ |
| Bottom layer | $5\cdot10^{-5}$ m s$^{-1}$ | $5\cdot10^{-5}$ m s$^{-1}$ | $1\cdot10^{-5}$ m s$^{-1}$ | $1\cdot10^{-5}$ m s$^{-1}$ |

833